

# Picocavity-enhanced Raman Spectroscopy of Physisorbed H<sub>2</sub> and D<sub>2</sub> Molecules

Akitoshi Shiotari,<sup>1,\*</sup> Shuyi Liu,<sup>1,2</sup> George Trenins,<sup>3</sup> Toshiki Sugimoto,<sup>4</sup> Martin Wolf,<sup>1</sup> Mariana Rossi,<sup>3,†</sup> and Takashi Kumagai<sup>4,‡</sup>

<sup>1</sup>*Department of Physical Chemistry,  
Fritz-Haber Institute of the Max-Planck Society,  
Faradayweg 4-6, 14195 Berlin, Germany*

<sup>2</sup>*Wuhan National Laboratory for Optoelectronics,  
Huazhong University of Science and Technology, Wuhan, China*

<sup>3</sup>*Max-Planck-Institute for Structure and Dynamics of Matter, 22761 Hamburg, Germany*

<sup>4</sup>*Institute for Molecular Science, National Institutes  
of Natural Sciences, 444-8585 Okazaki, Japan*

(Dated: November 19, 2024)

## Abstract

We report on tip-enhanced Raman scattering (TERS) of H<sub>2</sub> and D<sub>2</sub> molecules physisorbed within a plasmonic picocavity at a cryogenic temperature (10 K). The intense Raman peaks resulting from the rotational and vibrational transitions are observed at sub-nanometer gap distances of the junction formed by a Ag tip and Ag(111) surface. We clarify that the predominant contribution of the electromagnetic field enhancement of the picocavity to the detection of a single hydrogen molecule. The gap-distance dependent TERS reveals not only the evolution of the picocavity field, but also the interaction between the molecule and tip/surface, which exhibit nontrivial isotope effects. A significant red-shift and peak broadening of the H–H stretching as the gap distance decreases, while the D–D stretching mode is unaffected. A combination of density functional theory and reduced-dimension models reveals that a distinct anharmonicity in the mode potential of H<sub>2</sub> is one cause of the anomalous red-shift, whereas D<sub>2</sub> has less anharmonicity due to the geometric isotope effect.

The adsorption of hydrogen molecules on solid surfaces is the first step in permeation for fuel storage [1], catalytic hydrogenation [2], hydrogen embrittlement [3], and nuclear-spin isomer conversion [4]. To understand and control the elementary processes in such physical and chemical phenomena, hydrogen adsorption has been intensively studied in surface science [5–7]. However, only a few methods can be used to characterize physisorption systems, such as hydrogen on coinage-metal surfaces [8–13], because cryogenic-temperature measurements are required due to the faint adsorption energy ( $< 100$  meV). Low-temperature scanning tunneling microscopy (LT-STM) has been employed to investigate the dynamics of hydrogen molecules weakly adsorbed on surfaces [14–23]. Several studies have assigned characteristic features in conductance spectra to the rotational mode of hydrogen in the tip–sample junction [17–20]. However, the interpretation of the conductance spectra remains controversial; the features within the corresponding energy range [30–60 meV ( $\sim 240$ – $480$   $\text{cm}^{-1}$ ) for  $\text{H}_2$ ] could be attributed to configuration switches [14, 24, 25], to a molecule–substrate stretching mode [26], or to multiple phonon excitation [27]. Additionally, LT-STM studies have not provided information on the interatomic stretching mode of the molecule. Therefore, an alternative approach is required to identify the rotational/vibrational state.

Raman spectroscopy is a promising technique for characterizing hydrogen molecules on surfaces since the rotational and vibrational transitions of a homonuclear diatomic molecules are observable. However, the detection demands exceptional sensitivity due to the intrinsically small cross-section. Recent advancements in tip-enhanced and surface-enhanced Raman spectroscopy (TERS/SERS) have enabled the detection of single molecules [28–31]. Picocavities, atomic-scale protrusions present in plasmonic nanojunctions, play a crucial role in achieving extreme confinement of the electromagnetic field to Ångström scales [31–33], resulting in a significant enhancement of Raman scattering and ultrahigh spatial resolution [34–37]. So far, the exceptional sensitivity in TERS/SERS has been demonstrated primarily for organic molecules chemisorbed onto the substrate, where the enhancement benefits from chemical effects arising from the molecule–surface (and molecule–tip) interactions [38]. Therefore, applying TERS/SERS to physisorbed systems is not straightforward, as it depends on the fundamental enhancement mechanisms of Raman scattering in plasmonic picocavities.

Here we demonstrate that LT-TERS can observe single hydrogen molecules physisorbed onto an Ag(111) surface with an Ag tip [Fig. 1(a), inset], identifying their rotational and

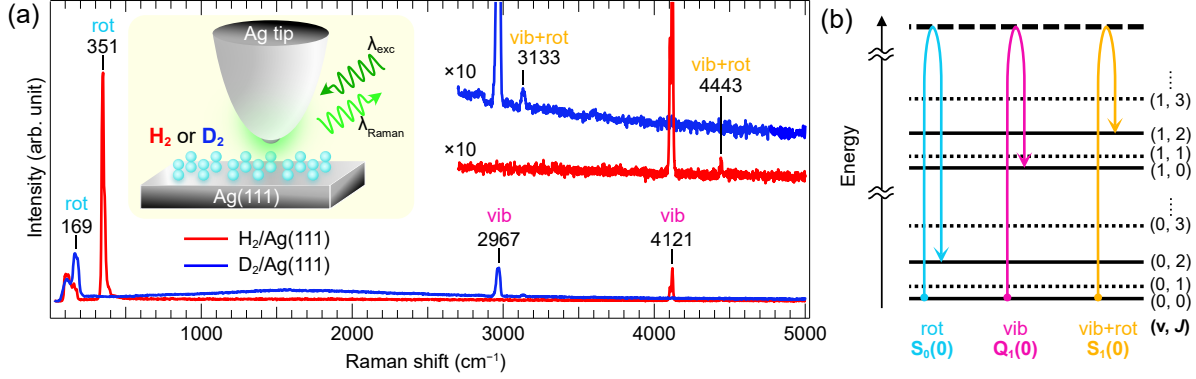


FIG. 1. (a) TERS spectra of  $\text{H}_2$  (red) and  $\text{D}_2$  (blue) on  $\text{Ag}(111)$  with a  $\text{Ag}$  tip at 10 K (sample bias voltage  $V_s = 10$  mV, and tunneling current  $I_t = 1.0$  nA). The left inset shows a schematic of the experiment.  $\lambda_{\text{exc(Raman)}}$  denotes the wavelength of the illumination laser (Raman scattering). The right inset shows magnified spectra at the high wavenumber regions. (b) Energy diagram of the vibrational and rotational levels of a  $\text{H}_2/\text{D}_2$  molecule. The solid (dotted) lines represent the levels for *para*- $\text{H}_2$  and *ortho*- $\text{D}_2$  (*ortho*- $\text{H}_2$  and *para*- $\text{D}_2$ ). The dashed bold line represents a virtual state. The arrows indicate Raman-active transitions of  $S_0(0)$ ,  $Q_1(0)$ , and  $S_1(0)$ , which are referred to as “rot,” “vib,” and “rot+vib,” respectively, for simplicity.

vibrational states. Furthermore, precise gap-distance control enables us to investigate not only how the picocavity field contributes to the Raman scattering process but also how the subtle van der Waals (vdW) interactions between the molecule and the tip/surface affect the anharmonicity of the potential energy surfaces and the accompanying nuclear quantum effects.

The LT-TERS experiments were performed in an ultra-high vacuum chamber, as described in the Supplemental Material (SM) [39]. The 532-nm incident laser beam was linearly polarized along the tip axis and focused on the apex of a focused-ion-beam-sharpened  $\text{Ag}$  tip [40] using an *in-situ* parabolic mirror, and the scattering light was detected by an *ex-situ* spectrometer. We performed density functional theory (DFT) calculations [41, 42] on a model geometry setup. We considered  $\text{H}_2/\text{D}_2$  on a  $4 \times 4$   $\text{Ag}(111)$  (periodic) surface, employing the Perdew-Burke-Ernzerhof (PBE) exchange-correlation functional and screened pairwise vdW interactions [43] (see SM [39] for details). The preferred adsorption sites (fcc/hcp hollow) and binding energies ( $\sim 30$  meV) were in very good agreement with previous studies of isolated molecules on the surface [44, 45]. A single  $\text{H}_2/\text{D}_2$  molecule proved

not to be stable in our simulations, due to the extremely low diffusion barrier. Therefore, we considered a coverage of 0.69 monolayer (ML), motivated by the results of path-integral molecular dynamics simulations at LT, where a 1 ML coverage was also unstable (see Section I-B in SM [39]). In 0.69 ML, the intermolecular attractive interaction increases the binding energy by 55 meV (Fig. S3 [39]). Over the sample, we put a Ag<sub>19</sub> cluster in a cleaved pyramidal geometry as a Ag tip (see Section I-B in SM [39] and Refs. [36, 46] for the tip structure details).

H<sub>2</sub> or D<sub>2</sub> gas was dosed into the chamber where a clean Ag(111) surface was cooled at 10 K. Regardless of laser illumination, hydrogen molecules on the surface are invisible with LT-STM (Fig. S1 [39]). In contrast, clear peaks were observed in TERS spectra under these conditions. Figure 1(a) displays a typical TERS spectrum of H<sub>2</sub> (D<sub>2</sub>) on Ag(111), showing two intense peaks at 351 (169) and 4121 (2967) cm<sup>-1</sup> together with a weak peak at 4443 (3133) cm<sup>-1</sup>. The three peaks in the TERS spectra can be assigned to rotational/vibrotational modes of hydrogen. Note that broad or asymmetric peak shapes are artifacts in the wide wavenumber range spectra (see Section I-A in SM [39]); higher resolution spectra will be shown later. The structure at ~100 cm<sup>-1</sup> common to the two spectra originates from Ag phonon modes of the tip [36, 47]. Figure 1(b) depicts the energy diagram of rotational/vibrational levels and possible transitions under the Raman selection rule [the change of the vibrational (rotational) quantum numbers  $\nu$  ( $J$ ) from the initial to final states should be 0 or  $\pm 1$  (0 or  $\pm 2$ )]. The observed peaks, in order from lowest to highest, correspond to the lowest-energy rotational transition [ $S_0(0)$ ; “rot” labeled in Fig. 1(a)], the lowest-energy vibrational transition [ $Q_1(0)$ ; “vib”], and their combination [ $S_1(0)$ ; “rot+vib”], respectively. The three modes were also detected in high-resolution electron energy loss spectroscopy (HREELS) of hydrogen on a polycrystalline Ag film [8] and a Cu(001) surface [9] at approximately 10–12 K; however, better energy resolution ( $<10$  cm<sup>-1</sup>) in TERS than that of the HREELS ( $>28$  cm<sup>-1</sup> [9]) makes the red-shifts from gas-phase hydrogen more discernible (Table S2). We should also note that only the stable nuclear spin isomer of each isotope, i.e., *para*-H<sub>2</sub> and *ortho*-D<sub>2</sub> [ $J = \text{even}$ ; Fig. 1(b)], is detected in TERS (Fig. S2). On the surface, the stable isomer is dominant due to the *ortho*–*para* conversion [4, 8, 44] (see SM [39] for details).

We calculate the H–H bonding distance to be 75.4 pm on Ag(111) (cf. 75.1 pm in the gas phase). Considering a rigid-rotor approximation, the rotational transition energy of *para*-H<sub>2</sub>

is calculated to be of  $353\text{ cm}^{-1}$  on the surface, compared to  $356\text{ cm}^{-1}$  in the gas phase. This is in good agreement with the experimental TERS peak at  $351\text{ cm}^{-1}$  (Fig. 1a) slightly red-shifted from  $354\text{ cm}^{-1}$  in the gas phase [48]. Notably, the H–H bonding distance of  $\text{H}_2$  on Ag(111) varied by only 0.06 pm at the closest tip position with respect to that without any tip included in our simulations. This suggests that the hydrogen molecules on the surface and in the STM junction behave as nearly free rotors.

In the harmonic approximation, the vibrational transition energy is calculated to be  $4318\text{ cm}^{-1}$  in the gas phase and  $4242\text{ cm}^{-1}$  on the surface (without the Ag tip). The experimental value in the gas phase is  $4161\text{ cm}^{-1}$  [48], and the harmonic equivalent, determined by fitting a harmonic potential to the bottom of the Morse-like potential, would correspond to  $4401\text{ cm}^{-1}$  [49]. The slight discrepancy between the experimental and calculated frequencies are in line with the usual spurious softening of the PBE functional. Well-known scaling factors can be applied to bring the harmonic numbers closer to the anharmonic ones for this simple molecule. The calculations indicate a red-shift of  $\sim 75\text{ cm}^{-1}$  upon the adsorption, which is larger but in reasonable agreement with the experimental TERS vibrational red-shift of  $\text{H}_2/\text{Ag}(111)$ . A simulated LT-TERS spectrum [46] is shown in Fig. S9 [39], which also agrees well with the experiment.

The TERS intensity is strongly correlated with the localized surface plasmonic resonance (LSPR) of the tip–sample junction. In general, there are two types of enhancement mechanisms effects in TERS [30, 38]: electromagnetic enhancement (originating from the LSPR of the junction with a plasmonic tip acting as an antenna for both incident light and Raman scattering) and chemical enhancement [originating from the interactions between the target molecule and the tip/surface]. In physisorption systems, the electromagnetic enhancement is expected to be dominant. We examined the excitation wavelength dependence (Fig. S10), verifying the contribution of LSPR to the TERS intensity; when the scattering light wavelength matches with the resonance range of the LSPR, strong TERS peak was observed.

The electromagnetic enhancement strongly depends on the cavity size. Figure 2(a) shows the gap-distance dependent TERS spectra recorded for  $\text{D}_2/\text{Ag}(111)$ . When the tip approaches the surface, the TERS intensities of the rotational and vibrational modes increase exponentially [Fig. 2(b)]. A broad background with a maximum at  $\sim 590\text{ nm}$  is attributed to electronic Raman scattering which represents the spectral response of the LSPR in the junction [50]. The gap-distance dependent intensities of both rotational and vibrational

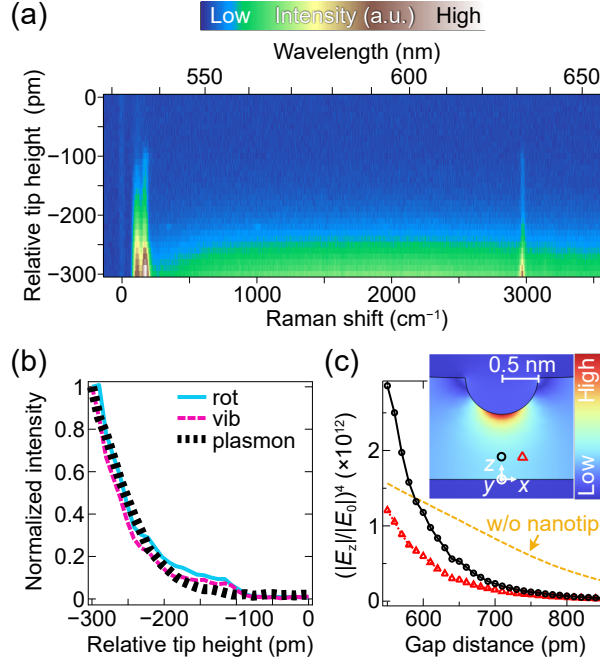


FIG. 2. (a) Waterfall plot for the TERS spectra during the tip approach to  $D_2/Ag(111)$ . The origin of the vertical axis corresponds to a tip height 100 pm higher than the STM setpoint at  $V_s = 10$  mV and  $I_t = 0.1$  nA. (b) Tip-height dependence of the Raman intensities, corresponding to the vertical line profiles of the rotational mode ( $168\text{ cm}^{-1}$ ), the vibrational mode ( $2968\text{ cm}^{-1}$ ), and the plasmonic background ( $2000\text{ cm}^{-1}$ ). The intensity is normalized for each profile. (c) Gap-distance dependence of the field enhancement factor simulated by FEM. The STM junction is modeled using a Ag tip (30-nm radius of curvature) with a nanotip (0.5-nm radius) and a flat Ag sample plate. The vertical electric field  $E_z$  at  $\lambda_{\text{exc}} = 532\text{ nm}$  is sampled and normalized with the incident field  $E_0$ . The inset shows the  $|E_z|$  distribution at a tip-sample gap distance of 0.9 nm. The black (red) curve represents the field enhancement factor  $(|E_z|/|E_0|)^4$  sampling at the location of the  $D_2$  just below the tip (the next neighboring  $D_2$  laterally separated by the Ag-Ag atomic distance), as indicated by the circle (triangle) marker in the inset. The orange curve represents the plot at the same sampling point as that for the black curve but using a Ag tip without a nanotip.

modes are in good agreement with that of the plasmonic feature [Fig. 2(b)], indicating the dominant contribution of the gap-mode plasmon to the TERS enhancement.

The gap-distance dependence of the TERS intensities is well reproduced by simulating the electronic field distribution in the Ag-tip-Ag-surface junction using the finite element

method (FEM) (see SM [39] for details). In the model, we assume a nanotip (0.5-nm radius of curvature) attached to a blunt tip body [51]. The black curve in Fig. 2(c) shows the field enhancement sampling at the position of a  $D_2$  molecule located under the Ag tip, indicating an exponential enhancement as the tip approaches. We confirmed the critical role of this sub-nanometric structure in TERS; as shown by the orange curve in Fig. 2(c), the tip without the nanotip exhibits a more moderate increase of the field enhancement as the tip approaches, which does not fit the experimental data [Fig. 2(b)]. The red curve in Fig. 2(c) shows the field enhancement at a possible position of the nearest neighboring molecule [Fig. 2(c), inset], indicating much lower enhancement. Therefore, TERS will have “nearly” single-molecule sensitivity, even for the physisorption system.

The rotational/vibrational spectroscopy is sensitive to the interaction between a target molecule and a local environment. We examine how the picocavity influences the rotational/vibrational state of  $H_2$  and  $D_2$ . Figures 3(a)–3(d) show the gap-distance dependence of high-resolution TERS spectra focusing on the rotational/vibrational modes of  $H_2/D_2$ ; notably, only the vibrational frequency of  $H_2$  exhibits a significant change [Fig. 3(c)]. Figure 3(e) shows the TERS spectra at three tip heights marked by the arrows in Fig. 3(c), indicating the red-shift and peak broadening as the gap distance decreases. Peak-fitting analysis for  $H_2$  [red dotted curve in Fig. 3(f)] indicates a corresponding peak shift of  $-34 \text{ cm}^{-1}$  with a 200 pm displacement of the tip, while it is only  $-3 \text{ cm}^{-1}$  for  $D_2$  (blue dotted curve). On the other hand, the rotational modes for both  $H_2$  and  $D_2$  [red and blue solid curves in Fig. 3(f), respectively] are almost unchanged, in good agreement with the calculated interatomic distance independent of the tip height as described above.

The significant (almost negligible) change of the vibrational mode of  $H_2$  ( $D_2$ ) can be explained by the anharmonicity of the potential energy surface (PES) of the molecule in the picocavity. The mode softening (red-shift and broadening) is associated with the PES of the molecule–surface distance, which is modified by the gap distance through the vdW interaction with the tip. Red-/Blue-shift of the intramolecular stretching mode through the vdW interaction has been reported by far-field Raman spectroscopy of hydrogen molecules physisorbed on carbon nanotubes [52]. The PES modification by the tip proximity was already reported for Au-tip- $H_2$ -Au-surface junction [53]; however, we clarified that the intermolecular interactions also play an important role in the PES shape (Figs. S4–S6 [39]). Since  $H_2$  has a higher zero-point energy (ZPE) than  $D_2$ , their vibrational frequencies can

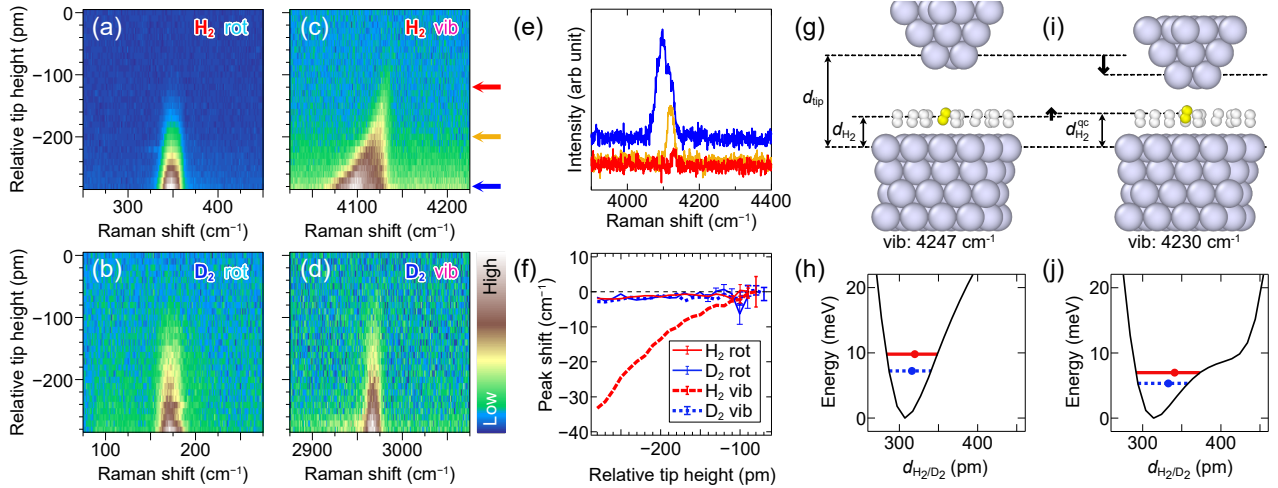


FIG. 3. (a,b) Waterfall plots of the high-resolution TERS spectra at the rotational mode regions for  $\text{H}_2$  and  $\text{D}_2$  on  $\text{Ag}(111)$ , respectively, with respect to the relative tip height. (c,d) The same as in (a) and (b), respectively, but at the vibrational mode regions. The origin of the relative tip height for  $\text{H}_2$  ( $\text{D}_2$ ) corresponds to a tip height 30 (70) pm higher than the setpoint at  $V_s = 10$  mV and  $I_t = 0.1$  nA. (e) TERS spectra of  $\text{H}_2/\text{Ag}(111)$ , corresponding to the horizontal line profiles in (c) indicated by the arrows in the same color. (f) Tip-height dependence of the peak position relative to that at a tip height of  $-110$  pm. It was obtained by fitting the spectrum at each height to a Gaussian peak with a constant background. The error bars indicate the standard deviation of the fitting, and those less than  $1.7 \text{ cm}^{-1}$  are not shown for clarity. (g) Simulated atomic structure of the junction at  $d_{\text{tip}} = 0.94$  nm. The light-blue, yellow, and white spheres represent Ag atoms, H atoms of  $\text{H}_2$  directly under the tip, and H atoms of the others, respectively.  $d_{\text{H}_2}$  denotes the distance between the  $\text{H}_2$  just under the tip and the topmost layer of  $\text{Ag}(111)$ . The calculated H–H stretching frequency is shown in the bottom of the panel. (h) PES of the molecule–surface distance at  $d_{\text{tip}} = 0.94$  nm. The red solid (blue dotted) line represents the ZPE of the  $\text{H}_2$  ( $\text{D}_2$ ) molecule under the tip. The bullet on each line indicates the quantum-corrected molecular height  $d_{\text{H}_2/\text{D}_2}^{\text{qc}}$ , where the quantum mechanical ZPE contributions at the PES was considered. (i, j) The same as in (g) and (h), respectively, but at  $d_{\text{tip}} = 0.74$  nm.

be more affected by the PES modification. Anharmonicity may also modify the lifetime of molecular vibrations [54, 55], which could lead to the peak broadening. However, the influence of neighboring molecules may not be negligible [Fig. 2(c)], which would contribute



to a shoulder at a lower frequency side of the vibrational peak [Fig. 3(e)].

To gain further insights into the observed red-shift, we calculated the PES experienced by the H<sub>2</sub>/D<sub>2</sub> molecules directly under the tip at several gap distances  $d_{\text{tip}}$ . The PES is obtained by calculating the total energies by moving the molecule at several molecule–surface distances  $d_{\text{H}_2/\text{D}_2}$  in the gap while the other atoms are fixed after the DFT optimization. The calculated PES exhibits a transition from a Morse-like potential [Fig. 3(h)] to an asymmetric double-well potential [Fig. 3(j)] as the gap distance decreases (see also Figs. S4 and S5). The quantum-corrected position  $d_{\text{H}_2/\text{D}_2}^{\text{qc}}$  for the H<sub>2</sub>/D<sub>2</sub> molecule directly under the tip is obtained by solving the one-dimensional Schrödinger equation in the sinc-function discrete-variable representation (see detailed method, Fig. S6, and Table S1 in SM [39]). In parallel, we calculated the vibrational frequency of H<sub>2</sub>/D<sub>2</sub> at each  $d_{\text{tip}}$  and  $d_{\text{H}_2/\text{D}_2}$  with the i-PI code [56]. We found a hallmark of vibrational coupling, i.e.,  $d_{\text{H}_2/\text{D}_2}$ -dependent vibrational frequencies (Figs. S7 and S8). Figure 3(g) [3(i)] shows  $d_{\text{H}_2}^{\text{qc}}$  at  $d_{\text{tip}} = 0.94$  [0.74] nm, where the stretching frequency is calculated to be 4247 [4230] cm<sup>-1</sup>. At the far [close] tip distance,  $d_{\text{H}_2}$  is calculated to be 320 [341] pm, while  $d_{\text{D}_2} = 316$  [333] pm, as shown in Fig. 3(h) [3(i)]. This indicates that D<sub>2</sub> is closer to the surface and farther from the tip than H<sub>2</sub>, due to the ZPE difference, and that both H<sub>2</sub> and D<sub>2</sub> molecules are slightly attracted toward the tip by the  $d_{\text{tip}}$  change from 0.94 to 0.74 nm. By the tip proximity, we predict  $\sim 18$  cm<sup>-1</sup> red-shift for H<sub>2</sub>, but only 9 cm<sup>-1</sup> red-shift for D<sub>2</sub>. This result is qualitatively consistent with the experiment, but under(over)estimates the red-shift for H<sub>2</sub> (D<sub>2</sub>). The absolute gap distance may be one of the possible reasons for this discrepancy; the gap distance in the experiment will be slightly different between H<sub>2</sub> and D<sub>2</sub> even with the same STM setpoint because of different tip-apex geometries. Finally, because the calculations regard the quantum-mechanical electronic ground-state only, we cannot rule out that non-adiabatic effects in the junction could further influence the observed isotopic differences in the TERS spectra. Such an analysis will be the subject of future work.

With LT-TERS, we observed the rotational/vibrational transitions of single hydrogen molecules through the interaction with the picocavity field. Our results suggest that LT-TERS is applicable to weakly adsorbed molecules, offering deeper insights into the local structures, reactions, and dynamics of adsorbates, such as chemical reactions at active sites [57] and surface diffusion (spillover) in catalytic processes [58], at the single-molecule level.

We thank Adnan Hammud for the Ag-tip fabrication. We thank Jun Yoshinobu and Heiko

Appel for helpful discussions. T.S. acknowledges the support of JST FOREST Grant No. JPMJFR221U. T.K. acknowledges the support of JST FOREST Grant No. JPMJFR201J and JSPS KAKENHI Grant No. JP19K24684.

---

\* Corresponding author: shiotari@fhi-berlin.mpg.de

† Corresponding author: mariana.rossi@mpsd.mpg.de

‡ Corresponding author: kuma@ims.ac.jp

- [1] N. W. Ockwig and T. M. Nenoff, Membranes for hydrogen separation, *Chem. Rev.* **107**, 4078 (2007).
- [2] L. Zhang, M. Zhou, A. Wang, and T. Zhang, Selective hydrogenation over supported metal catalysts: from nanoparticles to single atoms, *Chem. Rev.* **120**, 683 (2019).
- [3] X. Li, X. Ma, J. Zhang, E. Akiyama, Y. Wang, and X. Song, Review of hydrogen embrittlement in metals: hydrogen diffusion, hydrogen characterization, hydrogen embrittlement mechanism and prevention, *Acta Metallurgica Sinica* **33**, 759 (2020).
- [4] K. Fukutani and T. Sugimoto, Physisorption and ortho–para conversion of molecular hydrogen on solid surfaces, *Prog. Surf. Sci* **88**, 279 (2013).
- [5] K. Christmann, Interaction of hydrogen with solid surfaces, *Surf. Sci. Rep.* **9**, 1 (1988).
- [6] G. Vidali, G. Ihm, H.-Y. Kim, and M. W. Cole, Potentials of physical adsorption, *Surf. Sci. Rep.* **12**, 135 (1991).
- [7] L. Bruch, R. Diehl, and J. Venables, Progress in the measurement and modeling of physisorbed layers, *Rev. Mod. Phys.* **79**, 1381 (2007).
- [8] P. Avouris, D. Schmeisser, and J. Demuth, Observation of rotational excitations of H<sub>2</sub> adsorbed on Ag surfaces, *Phys. Rev. Lett.* **48**, 199 (1982).
- [9] S. Andersson and J. Harris, Observation of rotational transitions for H<sub>2</sub>, D<sub>2</sub>, and HD adsorbed on Cu(100), *Phys. Rev. Lett.* **48**, 545 (1982).
- [10] C.-f. Yu, K. B. Whaley, C. S. Hogg, and S. J. Sibener, Selective adsorption resonances in the scattering of *n*-H<sub>2</sub>, *p*-H<sub>2</sub>, *n*-D<sub>2</sub> and *o*-D<sub>2</sub> from Ag(111), *Phys. Rev. Lett.* **51**, 2210 (1983).
- [11] G. Anger, A. Winkler, and K. Rendulic, Adsorption and desorption kinetics in the systems H<sub>2</sub>/Cu(111), H<sub>2</sub>/Cu(110) and H<sub>2</sub>/Cu(100), *Surf. Sci.* **220**, 1 (1989).
- [12] K. Fukutani, K. Yoshida, M. Wilde, W. Diño, M. Matsumoto, and T. Okano, Photostimulated

- desorption and ortho-para conversion of H<sub>2</sub> on Ag surfaces, *Phys. Rev. Lett.* **90**, 096103 (2003).
- [13] K. Niki, T. Kawauchi, M. Matsumoto, K. Fukutani, and T. Okano, Mechanism of the ortho-para conversion of hydrogen on Ag surfaces, *Phys. Rev. B* **77**, 201404(R) (2008).
- [14] J. Gupta, C. Lutz, A. Heinrich, and D. Eigler, Strongly coverage-dependent excitations of adsorbed molecular hydrogen, *Phys. Rev. B* **71**, 115416 (2005).
- [15] R. Temirov, S. Soubatch, O. Neucheva, A. C. Lassise, and F. S. Tautz, A novel method achieving ultra-high geometrical resolution in scanning tunnelling microscopy, *New J. Phys.* **10**, 053012 (2008).
- [16] C. Lotze, M. Corso, K. J. Franke, F. von Oppen, and J. I. Pascual, Driving a macroscopic oscillator with the stochastic motion of a hydrogen molecule, *Science* **338**, 779 (2012).
- [17] S. Li, A. Yu, F. Toledo, Z. Han, H. Wang, H. He, R. Wu, and W. Ho, Rotational and vibrational excitations of a hydrogen molecule trapped within a nanocavity of tunable dimension, *Phys. Rev. Lett.* **111**, 146102 (2013).
- [18] F. D. Natterer, F. Patthey, and H. Brune, Distinction of nuclear spin states with the scanning tunneling microscope, *Phys. Rev. Lett.* **111**, 175303 (2013).
- [19] F. D. Natterer, F. Patthey, and H. Brune, Resonant-enhanced spectroscopy of molecular rotations with a scanning tunneling microscope, *ACS Nano* **8**, 7099 (2014).
- [20] A. J. Therrien, A. Pronschinske, C. Murphy, E. A. Lewis, M. L. Liriano, M. D. Marcinkowski, and E. C. H. Sykes, Collective effects in physisorbed molecular hydrogen on Ni/Au(111), *Phys. Rev. B* **92**, 161407(R) (2015).
- [21] S. Liu, A. Shiotari, D. Baugh, M. Wolf, and T. Kumagai, Enhanced resolution imaging of ultrathin ZnO layers on Ag(111) by multiple hydrogen molecules in a scanning tunneling microscope junction, *Phys. Rev. B* **97**, 195417 (2018).
- [22] L. Wang, Y. Xia, and W. Ho, Atomic-scale quantum sensing based on the ultrafast coherence of an H<sub>2</sub> molecule in an STM cavity, *Science* **376**, 401 (2022).
- [23] L. Wang, D. Bai, Y. Xia, and W. Ho, Electrical manipulation of quantum coherence in a two-level molecular system, *Phys. Rev. Lett.* **130**, 096201 (2023).
- [24] W. Thijssen, D. Djukic, A. Otte, R. Bremmer, and J. van Ruitenbeek, Vibrationally induced two-level systems in single-molecule junctions, *Phys. Rev. Lett.* **97**, 226806 (2006).
- [25] A. Halbritter, P. Makk, S. Csonka, and G. Mihály, Huge negative differential conductance in Au-H<sub>2</sub> molecular nanojunctions, *Phys. Rev. B* **77**, 075402 (2008).

- [26] Y. Li, S. Kaneko, S. Fujii, and M. Kiguchi, Symmetry of single hydrogen molecular junction with Au, Ag, and Cu electrodes, *J. Phys. Chem. C* **119**, 19143 (2015).
- [27] M. Trouwborst, E. Huisman, S. van der Molen, and B. van Wees, Bistable hysteresis and resistance switching in hydrogen-gold junctions, *Phys. Rev. B* **80**, 081407(R) (2009).
- [28] S.-Y. Ding, J. Yi, J.-F. Li, B. Ren, D.-Y. Wu, R. Panneerselvam, and Z.-Q. Tian, Nanostructure-based plasmon-enhanced Raman spectroscopy for surface analysis of materials, *Nat. Rev. Mater.* **1**, 16021 (2016).
- [29] X. Wang, S.-C. Huang, S. Hu, S. Yan, and B. Ren, Fundamental understanding and applications of plasmon-enhanced Raman spectroscopy, *Nat. Rev. Phys.* **2**, 253 (2020).
- [30] T. I. Itoh, M. Procházka, Z.-C. Dong, W. Ji, Y. S. Yamamoto, Y. Zhang, and Y. Ozaki, Toward a new era of SERS and TERS at the nanometer scale: From fundamentals to innovative applications, *Chem. Rev.* **123**, 1552 (2023).
- [31] C. Höppener, J. Aizpurua, H. Chen, S. Gräfe, A. Jorio, S. Kupfer, Z. Zhang, and V. Deckert, Tip-enhanced Raman scattering, *Nat. Rev. Methods Primers* **4**, 47 (2024).
- [32] F. Benz, M. K. Schmidt, A. Dreismann, R. Chikkaraddy, Y. Zhang, A. Demetriadou, C. Carnegie, H. Ohadi, B. De Nijs, R. Esteban, J. Aizpurua, and J. J. Baumberg, Single-molecule optomechanics in “picocavities”, *Science* **354**, 726 (2016).
- [33] M. Urbietta, M. Barbry, Y. Zhang, P. Koval, D. Sánchez-Portal, N. Zabala, and J. Aizpurua, Atomic-scale lightning rod effect in plasmonic picocavities: A classical view to a quantum effect, *ACS Nano* **12**, 585 (2018).
- [34] R. Zhang, Y. Zhang, Z. Dong, S. Jiang, C. Zhang, L. Chen, L. Zhang, Y. Liao, J. Aizpurua, Y. Luo, J. L. Yang, and J. G. Hou, Chemical mapping of a single molecule by plasmon-enhanced Raman scattering, *Nature* **498**, 82 (2013).
- [35] J. Lee, K. T. Crampton, N. Tallarida, and V. A. Apkarian, Visualizing vibrational normal modes of a single molecule with atomically confined light, *Nature* **568**, 78 (2019).
- [36] S. Liu, F. P. Bonafe, H. Appel, A. Rubio, M. Wolf, and T. Kumagai, Inelastic light scattering in the vicinity of a single-atom quantum point contact in a plasmonic picocavity, *ACS Nano* **17**, 10172 (2023).
- [37] J. Xu, X. Zhu, S. Tan, Y. Zhang, B. Li, Y. Tian, H. Shan, X. Cui, A. Zhao, Z. Dong, J. Yang, Y. Luo, B. Wang, and J. G. Hou, Determining structural and chemical heterogeneities of surface species at the single-bond limit, *Science* **371**, 818 (2021).

- [38] R. Chen and L. Jensen, Interpreting chemical enhancements of surface-enhanced Raman scattering, *Chem. Phys. Rev.* **4** (2023).
- [39] See Supplemental Material for detailed experimental and theoretical methods, additional figures, and tables, which includes Refs. [4, 8, 9, 12, 13, 16, 18, 19, 40–44, 46, 48, 51, 53, 56, 59–67].
- [40] S. Liu, B. Cirera, Y. Sun, I. Hamada, M. Müller, A. Hammud, M. Wolf, and T. Kumagai, Dramatic enhancement of tip-enhanced Raman scattering mediated by atomic point contact formation, *Nano Lett.* **20**, 5879 (2020).
- [41] V. Blum, R. Gehrke, F. Hanke, P. Havu, V. Havu, X. Ren, K. Reuter, and M. Scheffler, Ab initio molecular simulations with numeric atom-centered orbitals, *Comput. Phys. Commun.* **180**, 2175 (2009).
- [42] V. Gavini, S. Baroni, V. Blum, D. R. Bowler, A. Buccheri, J. R. Chelikowsky, S. Das, W. Dawson, P. Delugas, M. Dogan, C. Draxl, G. Galli, L. Genovese, P. Giannozzi, M. Giantomassi, X. Gonze, M. Govoni, F. Gygi, A. Gulans, J. M. Herbert, S. Kokott, T. D. Kühne, K.-H. Liou, T. Miyazaki, P. Motamarri, A. Nakata, J. E. Pask, C. Pleschl, L. E. Ratcliff, R. M. Richard, M. Rossi, R. Schade, M. Scheffler, O. Schütt, P. Suryanarayana, M. Torrent, L. Truflandier, T. L. Windus, Q. Xu, V. W.-Z. Yu, and D. Perez, Roadmap on electronic structure codes in the exascale era, *Model. Simul. Mat. Sci. Eng.* **31**, 063301 (2023).
- [43] V. G. Ruiz, W. Liu, E. Zojer, M. Scheffler, and A. Tkatchenko, Density-functional theory with screened van der Waals interactions for the modeling of hybrid inorganic-organic systems, *Phys. Rev. Lett.* **108**, 146103 (2012).
- [44] Y. Kunisada and H. Kasai, Hindered rotational physisorption states of H<sub>2</sub> on Ag(111) surfaces, *Phys. Chem. Chem. Phys.* **17**, 19625 (2015).
- [45] E. W. Smeets and G.-J. Kroes, Designing new SRP density functionals including non-local vdW-DF2 correlation for H<sub>2</sub> + Cu(111) and their transferability to H<sub>2</sub> + Ag(111), Au(111) and Pt(111), *Phys. Chem. Chem. Phys.* **23**, 7875 (2021).
- [46] Y. Litman, F. P. Bonafé, A. Akkoush, H. Appel, and M. Rossi, First-principles simulations of tip enhanced Raman scattering reveal active role of substrate on high-resolution images, *J. Phys. Chem. Lett.* **14**, 6850 (2023).
- [47] I. Pockrand and A. Otto, Surface enhanced raman scattering (SERS): Annealing the silver substrate, *Solid State Commun.* **38**, 1159 (1981).
- [48] D. K. Veirs and G. M. Rosenblatt, Raman line positions in molecular hydrogen: H<sub>2</sub>, HD, HT,

- D<sub>2</sub>, DT, and T<sub>2</sub>, *J. Mol. Spectrosc.* **121**, 401 (1987).
- [49] K. P. Huber and G. Herzberg, *Molecular spectra and molecular structure: Constants of diatomic molecules* (Van Nostrand, New York, 1979) pp. 716.
- [50] R. Kamimura, T. Kondo, K. Motobayashi, and K. Ikeda, Surface-enhanced electronic Raman scattering at various metal surfaces, *Phys. Status Solidi B* **259**, 2100589 (2022).
- [51] S. Liu, M. Müller, Y. Sun, I. Hamada, A. Hammud, M. Wolf, and T. Kumagai, Resolving the correlation between tip-enhanced resonance raman scattering and local electronic states with 1 nm resolution, *Nano Lett.* **19**, 5725 (2019).
- [52] K. A. Williams, B. K. Pradhan, P. C. Eklund, M. K. Kostov, and M. W. Cole, Raman spectroscopic investigation of H<sub>2</sub>, HD, and D<sub>2</sub> physisorption on ropes of single-walled, carbon nanotubes, *Phys. Rev. Lett.* **88**, 165502 (2002).
- [53] T. Sugimoto, Y. Kunisada, and K. Fukutani, Inelastic electron tunneling mediated by a molecular quantum rotator, *Phys. Rev. B* **96**, 241409(R) (2017).
- [54] B. Persson and R. Ryberg, Vibrational line shapes of low-frequency adsorbate modes: CO on Pt(111), *Phys. Rev. B* **40**, 10273 (1989).
- [55] H. Ueba, Vibrational lineshapes of adsorbates on solid surfaces, *Prog. Surf. Sci.* **22**, 181 (1986).
- [56] V. Kapil, M. Rossi, O. Marsalek, R. Petraglia, Y. Litman, T. Spura, B. Cheng, A. Cuzzocrea, R. H. Meißner, D. M. Wilkins, B. A. Helfrecht, P. Juda, S. P. Bienvenue, W. Fang, J. Kessler, I. Poltavsky, S. Vandenbrande, J. Wieme, C. Corminboeuf, T. D. Kühne, D. E. Manolopoulos, T. E. Markland, J. O. Richardson, A. Tkatchenko, G. A. Tribello, V. V. Speybroeck, and M. Ceriotti, i-PI 2.0: A universal force engine for advanced molecular simulations, *Comput. Phys. Commun.* **236**, 214 (2019).
- [57] Z.-F. Cai, N. Kumar, and R. Zenobi, Probing on-surface chemistry at the nanoscale using tip-enhanced Raman spectroscopy, *CCS Chem.* **5**, 55 (2023).
- [58] J.-L. Yang, Y.-W. Zhou, M.-Y. Jia, Q. Liu, and Z.-F. Cai, Insights into heterogeneous catalysis by tip-enhanced Raman spectroscopy, *ChemCatChem* **16**, e202400370 (2024).
- [59] R. L. Summers, Empirical observations on the sensitivity of hot cathode ionization type vacuum gages, NASA Technical Report **NASA-TN-D-5285** (1969).
- [60] J. Hermann and A. Tkatchenko, Density functional model for van der Waals interactions: Unifying many-body atomic approaches with nonlocal functionals, *Phys. Rev. Lett.* **124**, 146401 (2020).

- [61] C. Schwartz, High-accuracy approximation techniques for analytic functions, *J. Math. Phys.* **26**, 411 (1985).
- [62] D. T. Colbert and W. H. Miller, A novel discrete variable representation for quantum mechanical reactive scattering via the  $S$ -matrix Kohn method, *J. Chem. Phys.* **96**, 1982 (1992).
- [63] Y. Jiang, S. Pillai, and M. A. Green, Realistic silver optical constants for plasmonics, *Sci. Rep.* **6**, 30605 (2016).
- [64] B. Pettinger, Single-molecule surface- and tip-enhanced Raman spectroscopy, *Mol. Phys.* **108**, 2039 (2010).
- [65] L. Wolniewicz, The  $X^1\Sigma_g^+$  state vibration-rotational energies of the  $H_2$ , HD, and  $D_2$  molecules, *J. Chem. Phys.* **78**, 6173 (1983).
- [66] M. Sakurai, T. Okano, and Y. Tuzi, Ortho-para conversion of  $n$ - $H_2$  physisorbed on Ag(111) near two-dimensional condensation conditions, *Appl. Surf. Sci.* **33**, 245 (1988).
- [67] G. K. Teal and G. E. MacWood, The Raman spectra of the isotopic molecules  $H_2$ , HD, and  $D_2$ , *J. Chem. Phys.* **3**, 760 (1935).

# SUPPLEMENTAL MATERIAL: PICOCAVITY-ENHANCED RAMAN SPECTROSCOPY OF PHYSISORBED H<sub>2</sub> AND D<sub>2</sub> MOLECULES

## I. METHODS

### A. STM-TERS Experiments

The experiments were performed in an ultrahigh vacuum (UHV) chamber equipped with an STM-based TERS machine (modified UNISOKU USM-1400) at a sample temperature of 10 K. A single-crystalline Ag(111) surface (MaTeck) was cleaned by Ar-sputtering-and-annealing cleaning cycles in the chamber. H<sub>2</sub> ( $\geq 99.999\%$ , Westfalen AG) or D<sub>2</sub> (99.7%, Air Liquide) gas was dosed into the STM unit cooled at 10 K via a variable leak valve. The gas exposure (Langmuir; L) is estimated by  $Pt/n$ , where  $P$  [ $10^{-6}$  Torr],  $t$  [s], and  $n$  denote the displayed pressure value of the gauge (corrected by N<sub>2</sub>), the exposure duration, and the correction factor for the gauge. A Bayard-Alpert ionization gauge is located outside the cryogen-cooled STM unit in the chamber and  $n = 0.384$  (0.388) is used for H<sub>2</sub> (D<sub>2</sub>) [59]. We used a chemically-etched Ag tip that was sharpened by focused-ion-beam milling as described elsewhere [40]. The bias voltage  $V_s$  was applied to the sample while the tip was grounded. The STM images were obtained in the constant current mode at  $I_t = 50$  pA. The cleanness of the cleaned surface and tip was confirmed by STM images [Fig. S1(a)]. We also confirmed that a TERS spectrum of the Ag–Ag junction before hydrogen dosing had no molecule-derived peaks (Fig. S2, at 0 L)

In the STM junction,  $p$ -polarised visible laser (532-nm solid-state or 633-nm HeNe) was incident through a fused silica window and a Ag-coated parabolic mirror (numerical aperture of  $\sim 0.6$ ). The incident laser power is 5.9 (9.7) mW at  $\lambda_{\text{ext}} = 532$  (633) nm. The parabolic mirror is mounted on a five-axis piezoelectric-motor stage in the LT-STM unit and the laser is focused at the tip apex by adjusting the position and angle of the parabolic mirror. The scattered light corrected by the parabolic mirror was directed to a spectrometer (AndorShamrock 303i) outside the UHV chamber via a beam splitter and a longpass filter specific for each excitation wavelength. For the TERS and STM-induced luminescence (STML) spectra, we used the gratings 150 (for Fig. S3), 600 (Figs. 1, 2, and S2), and 1200 line/mm (Fig. 3). A sparser grating allows the acquisition of wider-wavelength range spectra, as shown in Fig. S3 (see Sec. II-B), but Raman peaks become broad and asymmetric.



Thus, for the high-frequency-resolution measurements shown in Fig. 3, the densest grating was used.

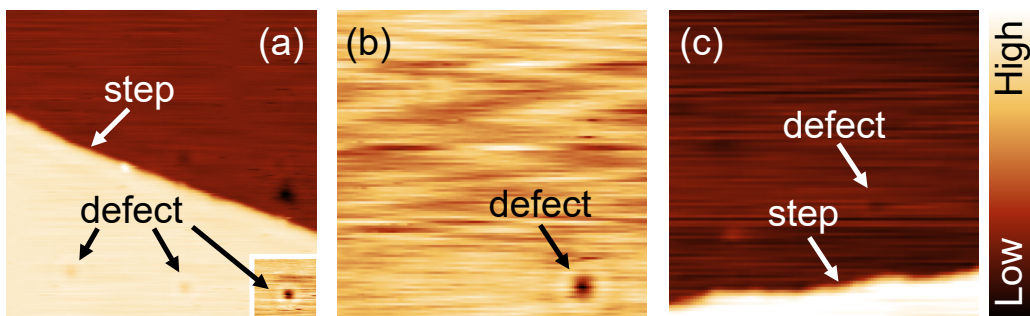


FIG. S1. (a)–(c) Typical STM images of a clean Ag(111) surface, H<sub>2</sub>/Ag(111), and D<sub>2</sub>/Ag(111), respectively [ $V_s = 0.1$  V,  $I_t = 0.1$  nA,  $T = 10$  K, exposure: H<sub>2</sub> 50 L for (b) and D<sub>2</sub> 220 L for (c), scan size:  $40 \times 40$  nm<sup>2</sup> for (a) and (c),  $24 \times 24$  nm<sup>2</sup> for (b)]. The TERS spectra of H<sub>2</sub>/Ag(111) and D<sub>2</sub>/Ag(111) shown in Fig. 1b of the main text were obtained with the same sample and tip as (b) and (c), respectively. The depressions observed in (b) and (c) are ascribed to subsurface point defects, which were also observed on a clean surface as shown in (a) and its inset STM image. Although the visibility of subnanoscale structures such as defects and single Ag atomic steps guarantees high spatial resolution imaging, we cannot find any hydrogen-derived feature with STM. Molecular hydrogen films were visualized only on a limited number of substrates [16, 18, 19] and no STM image of hydrogen molecules on the Ag surface has been reported.

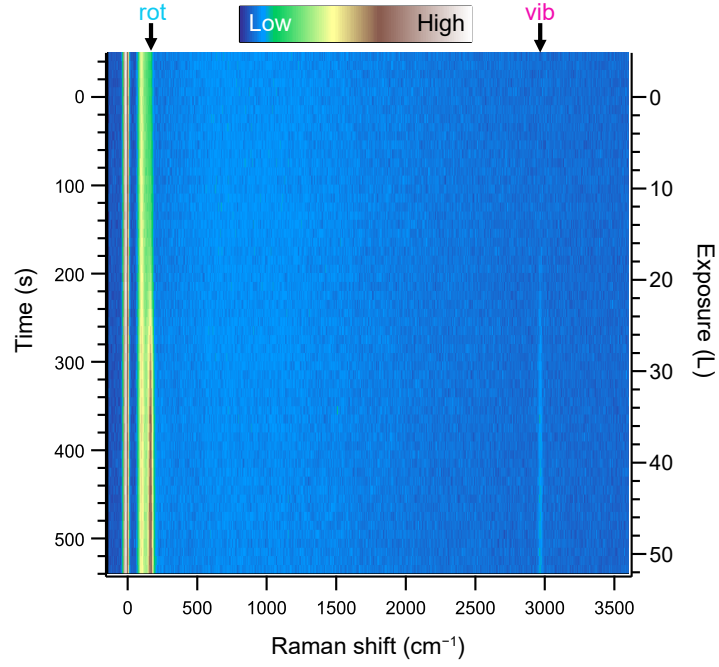


FIG. S2. Waterfall plot of TERS spectra of Ag(111) during  $D_2$  gas exposure ( $V_s = 0.01$  V,  $I_t = 1$  nA,  $T = 10$  K,  $\lambda_{exc} = 532$  nm, accumulation: 10 s/spectrum). The point at which the gas dose started is set as the origin of the time axis. The rot and vib modes of *ortho*- $D_2$  are indicated on top of the plot. The structure at  $\sim 100$   $cm^{-1}$  that was constantly observed before the gas dose is ascribed to the Ag phonon mode, as described in the main text.

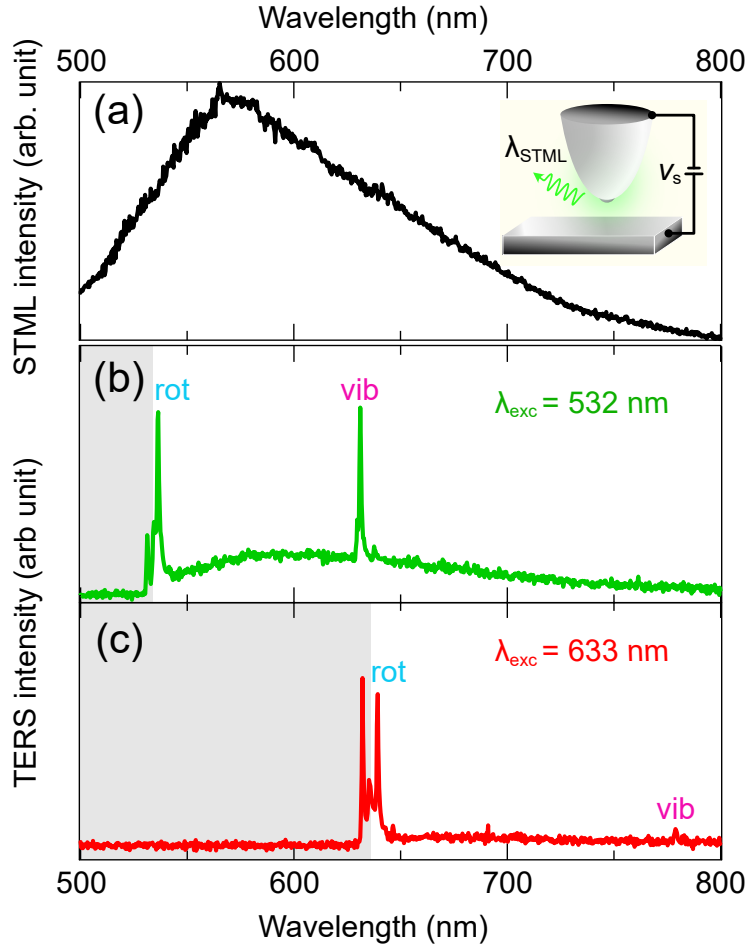


FIG. S3. Correlation between Raman scattering and plasmonic resonance in the STM junction. (a) STM luminescence (STML) spectrum recorded over a clean Ag(111) surface with a Ag tip ( $V_s = 3$  V,  $I_t = 5$  nA). The inset shows the schematic of the STML experiment. The horizontal axis is the luminescence wavelength  $\lambda_{\text{STML}}$ . After recording the spectrum, the surface was exposed to the  $D_2$  gas. (b and c) TERS spectra of  $D_2/\text{Ag}(111)$  with  $\lambda_{\text{exc}} = 532$  and 633 nm, respectively ( $V_s = 10$  mV,  $I_t = 1$  nA), using the Ag tip as for (a). The horizontal axis is indicated by wavelength  $\lambda_{\text{Raman}}$  instead of the Raman shift. The gray background represents the long-pass filtered region.

## B. DFT Calculations and Molecular Dynamics

DFT calculations were performed with the FHI-aims program package [41, 42]. We used intermediate defaults for basis sets, radial grids and cutoff potential parameters and light defaults for the Hartree multipole expansion and angular grids. This combination proved efficient and reliable against benchmarks to tight settings. We simulated an orthogonal  $4 \times 4$  Ag(111) surface cell oriented perpendicular to the  $z$  axis, containing four layers. The cell parameters used were  $a = 11.554 \text{ \AA}$ ,  $b = 10.007 \text{ \AA}$  and  $c = 65.000 \text{ \AA}$ . We employed a  $2 \times 2 \times 1$   $k$ -point grid and a dipole correction was employed to maximally decouple periodic images along the  $z$  direction. We used the PBE exchange-correlation functional and included vdW interactions through the pairwise screened TS-vdW<sup>surf</sup> method of Ref. [43] in all simulations reported in the main text. Figure S4 shows a comparison of binding energies with the many-body NL-MBD dispersion correction of Ref. [60], indicating a weaker binding energy by only 5 meV and a binding distance 0.1  $\text{\AA}$  closer to the surface. Structures were optimized by allowing only hydrogen molecules and the top layer of Ag atoms of the surface to relax. All the other atoms were kept fixed at their bulk (or tip) positions. When we performed simulations including a model tip structure, this was modeled by a Ag<sub>19</sub> cluster at varying distances from the surface. Although this tip size would not be sufficient to capture a proper plasmonic response of the tip, the tip structure can capture the local interactions close to the tip apex [36, 46].

We inspected binding sites and binding energies of a single adsorbed H<sub>2</sub> molecule, finding all values in good agreement with previous studies [44]. The binding energy was defined as the difference between the total energy when the molecule was 10  $\text{\AA}$  away from the surface and the minimum total energy of the adsorbed molecule. The blue curve in Fig. S4 shows the binding curve of a single H<sub>2</sub> molecule adsorbed on the fcc-hollow site of the Ag(111) surface, indicating an equilibrium H<sub>2</sub>-Ag(111) bonding length  $d_{\text{H}_2}^{\text{opt}}$  of 3.09  $\text{\AA}$  and a binding energy of 32 meV. The model we used in most simulations contained 11 molecules in the unit cell (see rationale below). For this molecular concentration, we evaluated the intermolecular interaction by comparing the binding curves (orange and green curves in Fig. S4) with that of the single-molecule case (blue); the molecule-molecule interaction in our models amounts to 55 meV/molecule.

Performing vibrational analysis on the optimized single molecule adsorbed on the sur-

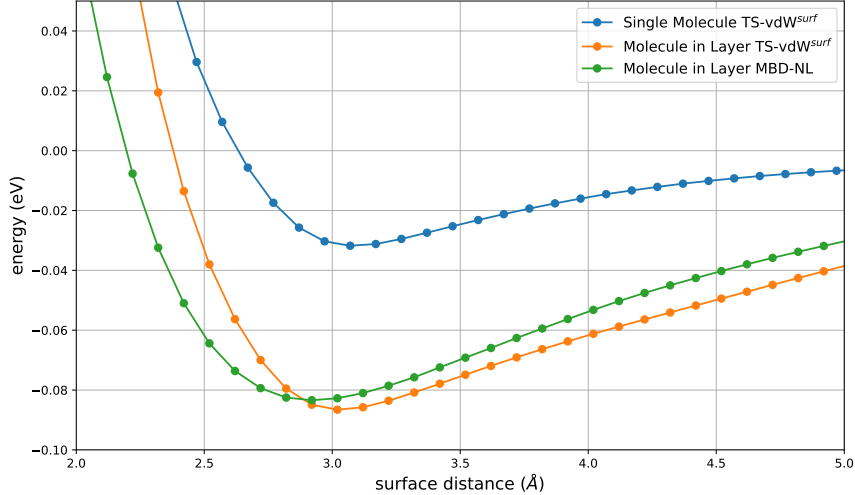


FIG. S4. Binding energies of  $\text{H}_2$  to the  $\text{Ag}(111)$  surface. The blue curve was (orange and green curves were) calculated using the unit cell with only one molecule (11 molecules), corresponding to  $\sim 0.06$  ( $\sim 0.69$ ) ML. The  $\text{TS-vdW}^{\text{surf}}$  (MBD-NL) dispersion interactions were used for the blue and orange curves (green curve). All corrections are added to the PBE functional. The origin of the vertical axis is set to the total energy when the molecule was  $10 \text{ \AA}$  away from the surface.

face showed that negative frequencies related to rotational and translational modes of the molecule were always present. This led us to consider higher coverages to model local stable clustering of the molecules on the surface. We considered a full monolayer (1 ML), where all fcc-hollow sites of the unit cell were occupied by  $\text{H}_2$ . With this setup we performed Born-Oppenheimer molecular dynamics (BOMD) and path-integral molecular dynamics (PIMD) at LT ( $T = 20 \text{ K}$ ) with the i-PI code [56] connected to FHI-aims. PIMD simulations used 12 beads in conjunction with a normal-mode colored-noise thermostat with 8 auxiliary variables and  $\hbar\omega/kT = 500$ . This number of beads is not fully converged at this temperature even with the colored-noise quantum thermostats, but the purpose of these simulations was exploratory.

While the full monolayer was stable during more than 10 ps on the classical trajectories, in the quantum trajectory 5 molecules readily desorbed (within the first picosecond) from the substrate. For the quantum case we validated this observation by simulating trajectories with a parameterized Lennard-Jones potential representing the  $\text{Ag}(111)$  surface. We could calculate the radius of gyration of H atoms from the PIMD simulations, belonging to the 3 molecules closest to the tip at any point in the simulation. For the closest tip distance

considered ( $d_{\text{tip}} = 7.4 \text{ \AA}$ ), these were  $0.33 \text{ \AA}$  along  $x$  and  $y$  and  $0.30 \text{ \AA}$  along  $z$  ( $T = 20 \text{ K}$ ), indicating a small anisotropy. Converting these numbers to an effective thermal de Broglie wavelength  $\Lambda$  and applying a inverse-square-root scaling for the temperature and mass, we would obtain  $\Lambda_H = 2.3 \text{ \AA}$  and  $\Lambda_D = 1.5 \text{ \AA}$  at  $10 \text{ K}$ . We note that, depending on the density of  $\text{H}_2$  molecules on the surface,  $\Lambda_{\text{H}_2}$  is about the length of the inter-particle spacing at  $10 \text{ K}$  and signatures of bosonic exchange could begin to be observed. These features are disregarded in the current simulations.

Figure S5 shows the energy profiles of a  $\text{H}_2$  molecule with varying distance to the Ag(111) surface at different tip-surface distances. We only varied the position of the molecule closest to the tip apex, while the others were kept at equilibrium [see also Figs. 3(g) and 3(i) in the main text]. The profile shapes are similar to an asymmetric double-well potential at closer tip-surface distances, while they assume a shape closer to a Morse potential at larger distances, which asymptotically approaches the profile of a  $\text{H}_2$  molecule on Ag(111) without the Ag tip (yellow curve in Fig. S5). The asymmetry of the double-well is strongly impacted by the presence of other molecules on the surface (molecule-molecule interactions). Figure S6 shows a comparison with the limiting case of a single molecule in the unit cell at a tip-surface distance of  $9.4 \text{ \AA}$ . In that case (orange curve), if the molecule can overcome the barrier, it will have a higher probability of being found closer to the tip, which was predicted in a Au-tip-single- $\text{H}_2$ -Au-surface junction [53].

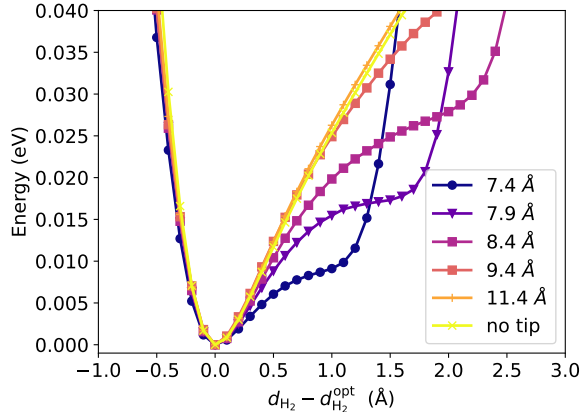


FIG. S5. Energy profiles of a  $\text{H}_2$  molecule with varying distance to the  $\text{Ag}(111)$  surface without (yellow curve) and with a  $\text{Ag}$  tip at different tip–surface distances (the other curves). All results obtained with the  $\text{PBE}+\text{TS-vdW}^{\text{surf}}$  exchange–correlation functional. For visual clarity, each curve was shifted so that the equilibrium  $\text{H}_2$ – $\text{Ag}(111)$  bonding distance  $d_{\text{H}_2}^{\text{opt}}$  and the bonding energy at each tip height is at the origin of the horizontal and vertical axes, respectively.

### C. Exact DVR Models and Vibrational Analysis

For the potentials shown in Fig. S5, we solved the one-dimensional Schrödinger equation exactly in the sinc-function discrete variable representation (DVR) [61, 62]. We set the mass of the hydrogen atom to  $m_{\text{H}} = 1836.1527 m_e$  and that of deuterium to  $m_{\text{D}} = 2m_{\text{H}}$ . In all cases, calculations were performed on a regularly spaced grid of 100 points, spanning values of  $(d_{\text{H}_2} - d_{\text{H}_2}^{\text{opt}})$  from  $-1.5$  to  $4.4 \text{ \AA}$  with a potential-energy cut-off  $V_c = 0.2 \text{ eV}$ . The potential energies used in the DVR were obtained from a cubic spline interpolation of the DFT-calculated values in Sec. I-B. The resulting ZPEs and average ground-state displacements of the molecular center of mass from equilibrium,

$$\Delta d_{\text{H}_2}^{\text{qc}} = d_{\text{H}_2}^{\text{qc}} - d_{\text{H}_2}^{\text{opt}} = \langle \psi_{0,\text{H}_2} | \hat{x} | \psi_{0,\text{H}_2} \rangle - d_{\text{H}_2}^{\text{opt}}, \quad (\text{S1})$$

are given in Table S1, as well as those for  $\text{D}_2$ . Here,  $d_{\text{H}_2}^{\text{qc}}$  is the molecular height considering the quantum mechanical ZPE contributions at the PES (i.e., the “quantum-corrected” molecular heights), and  $|\psi_{0,\text{H}_2}\rangle$  are the underlying ground-state wavefunctions, which are plotted in Fig. S7 to further illustrate the influence of tip–surface separation on the ZPEs and the equilibrium displacements.

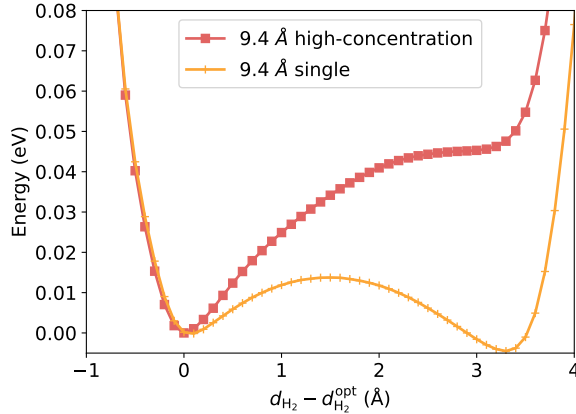


FIG. S6. Energy profiles of a  $\text{H}_2$  molecule with varying distance to the  $\text{Ag}(111)$  surface at a tip-surface distance of  $9.4 \text{ \AA}$ . The red and orange curves indicate the profiles with the higher concentration (11 molecules in the cell) and the lowest concentration (1 molecule in the cell), respectively. The origins of the axes are defined in the same manner as in Fig. S5.

TABLE S1. ZPEs and the average ground-state displacements of the molecular center of mass from equilibrium  $\Delta d_{\text{H}_2}^{\text{qc}}$  and  $\Delta d_{\text{D}_2}^{\text{qc}}$  calculated using DVR for  $\text{H}_2$  and  $\text{D}_2$  on  $\text{Ag}(111)$  at varying tip-surface distances  $d_{\text{tip}}$  and in the absence of a tip. All energies and distances are reported relative to the potential-energy minima and are converged at least to the quoted accuracy, as verified by comparing to values from a tighter grid of 400 regularly spaced points spanning  $-3.0$  to  $6.0 \text{ \AA}$  with an energy cut-off  $V_c = 1 \text{ eV}$ .

$d_{\text{tip}} [\text{\AA}]$	7.4	7.9	8.4	9.4	11.4	no tip
$\text{ZPE}_{\text{H}_2} [\text{meV}]$	6.9840	8.4652	9.0367	9.7890	9.7436	9.6820
$\text{ZPE}_{\text{D}_2} [\text{meV}]$	5.3070	6.3200	6.6741	7.2238	7.1378	7.0799
$\Delta d_{\text{H}_2}^{\text{qc}} [\text{\AA}]$	0.2684	0.1925	0.1545	0.1273	0.1273	0.1406
$\Delta d_{\text{D}_2}^{\text{qc}} [\text{\AA}]$	0.1874	0.1303	0.1083	0.0906	0.0917	0.1013

In parallel we conducted harmonic vibrational analysis with the i-PI code, varying the height of the  $\text{H}_2/\text{D}_2$  molecule directly under the tip apex  $d_{\text{H}_2/\text{D}_2}$  and varying the tip-sample distance  $d_{\text{tip}}$  [see also Figs. 3(g) and 3(i)]. Figures S8 and S9 show the dependence of the H-H and D-D stretching vibration on the mode corresponding to the vertical hindered translation of the adsorbed molecule, i.e.,  $\text{H}_2\text{-Ag}(111)$  and  $\text{D}_2\text{-Ag}(111)$ , respectively. At



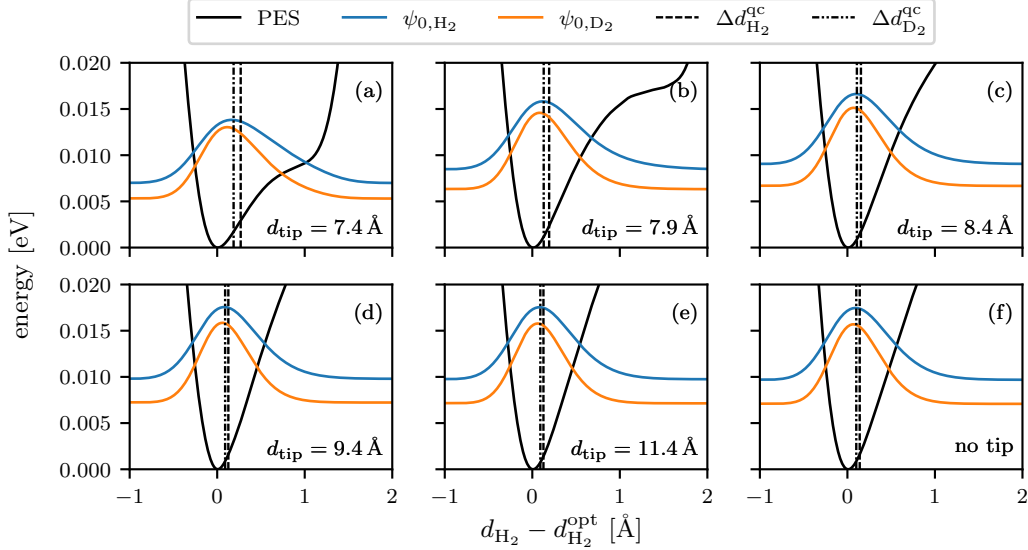


FIG. S7. Ground-state wavefunctions for  $\text{H}_2$  (blue) and  $\text{D}_2$  (orange) on  $\text{Ag}(111)$ , calculated for different tip–surface distances (a–e) and in the absence of a tip (f). In each case, the origin of the horizontal (vertical) axis is at the DFT-optimized position (energy). The black solid curves represent the PESs shown in Fig. S5.  $\Delta d_{\text{H}_2}^{\text{qc}}$  and  $\Delta d_{\text{D}_2}^{\text{qc}}$  are shown as dashed and dash-dotted vertical lines, respectively.

each  $d_{\text{H}_2/\text{D}_2}$ , there is a red-shift of the interatomic stretching frequency with approaching tip, which follows a  $\sqrt{2}$  mass scaling between  $\text{H}_2$  and  $\text{D}_2$ . As described above, with the DVR solutions, we obtain the the quantum-corrected molecule–surface distance  $d_{\text{H}_2/\text{D}_2}^{\text{qc}}$ . Based on the  $d_{\text{H}_2/\text{D}_2}$ -dependent vibrational frequency curves, we obtain the vibrational frequency at  $d_{\text{H}_2/\text{D}_2}^{\text{qc}}$ , as shown by the blue (green) squares for  $\text{H}_2$  ( $\text{D}_2$ ) in Fig. S8 (S9). The plot indicates an anomalous isotopic red-shift for  $\text{H}_2$  (factor 2, instead of  $\sqrt{2}$ ), stemming from the two following factors: (1) strong anharmonic character of the hindered translation of the molecule, which is dominated by the vdW interactions with the tip and the surface (see Fig. S5), and (2) the coupling of this mode with the vibrational stretching mode.

We stress that different heights of the tip and different concentrations of the molecules can exacerbate this effect. The former because the red-shift is more pronounced at closer tip distances than at larger tip distances. The latter because weaker binding energies to the surface at lower concentrations result in softer potentials that assume a double-well character at larger tip distances (see the orange curve in Fig. S6). This effect can result in a more pronounced negative slope of the dashed curves in Figs. S8 and S9. It is challenging

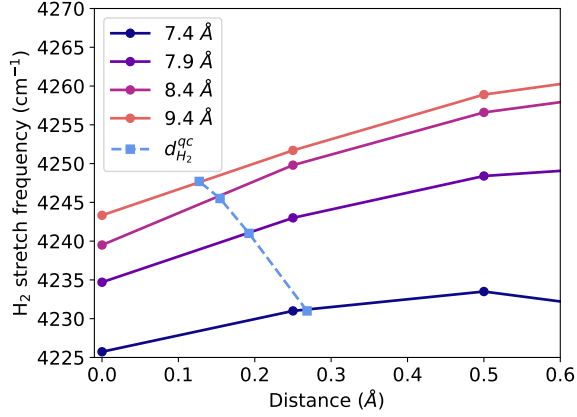


FIG. S8. Calculated interatomic stretching frequencies of the  $H_2$  molecule closest to the tip apex at different tip–surface distance  $d$  (different color curves) when varying the  $H_2$  molecular distance to the Ag(111) surface (horizontal axis;  $d_{H_2}$ ). The origin of the horizontal axis is set at the DFT-optimized position of each geometry. The quantum-corrected molecular position  $d_{H_2}^{qc}$  and corresponding vibrational frequency considering the quantum mechanical ZPE contributions at the hindered vertical translational coordinate at each geometry is marked by squares and connected by dashed lines as guides for the eye.

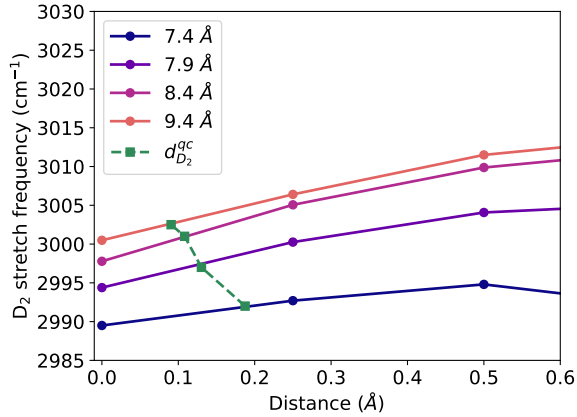


FIG. S9. Same as in Fig. S8 but for  $D_2$ .

to determine the local molecular concentration closer to the tip apex at any measurement and a deeper study of the vibrational frequency variation could provide indirect hints to the observed concentration. Although we neglected the anharmonic character of the H–H stretching coordinate in this study, we expect this effect not to change the qualitative

discussion and introduce only rigid red-shifts on the values reported here.

#### D. TERS Spectrum Simulation

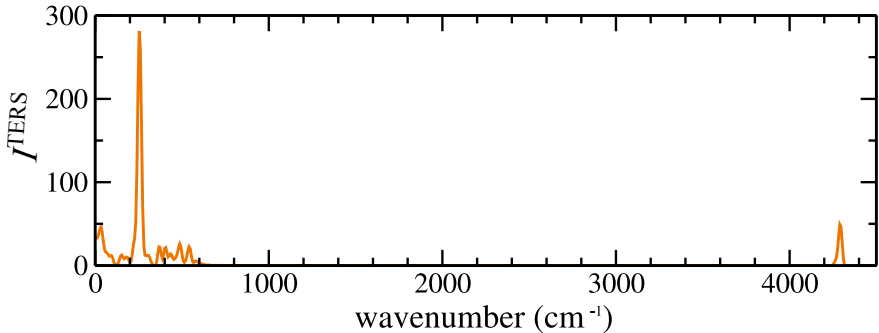


FIG. S10. Simulated anharmonic TERS spectrum of H<sub>2</sub> in a tip–surface junction.

We conducted TERS simulations according to the methodology proposed in Ref. [46]. We used Tip A discussed in the reference and calculated the anharmonic Raman spectrum based on a classical ab initio molecular dynamics (AIMD) trajectory (5 ps) of a molecular layer adsorbed on the surface and a tip apex located 4 Å above the molecular layer at  $T = 20$  K. We calculated the TERS intensity as  $I^{\text{TERS}} \propto \int dt e^{i\omega t} \langle \alpha_{zz}^{\text{local}}(0) \alpha_{zz}^{\text{local}}(t) \rangle$ , where  $\alpha_{zz}^{\text{local}}$  was obtained by a local polarizability calculation at each geometry in the time-series given by the molecular dynamics. For this part of the calculation we only considered the free-standing molecular layer (no surface) at the positions adopted in the AIMD trajectory including the surface. We note that the method of Ref. [46] is unable to capture the electromagnetic plasmonic enhancement in its totality. We do not observe any noteworthy features in the spectrum and it overall agrees with the experimental spectrum. The red-shift of the rotational band in the simulation is explained by the lack of consideration of the nuclear spin, making calculations reproduce only classical rotations that are red-shifted if compared to the quantized  $J = 0 \rightarrow 2$  transition of *para*-H<sub>2</sub>. This simulation had only an exploratory character and achieving statistical convergence through the use of parametrized machine-learned potentials, plus the inclusion of accurate plasmonic enhancements is beyond the scope of this paper.

## E. FEM Simulations

To evaluate the electric field in the STM junction, we performed finite element method (FEM) simulations using COMSOL Multiphysics (version 6.2 with the Wave Optics Module). We used the three-dimensional model with a Ag tip and Ag sample plate described in Supporting Information of Ref. [51]. As needed, at the apex of the Ag tip (a length of 300 nm, an effective radius of 30 nm), a half-sphere protrusion with a radius of 0.5 nm is attached as a “nanotip.” A  $p$ -polarized plane wave with  $\lambda_{\text{ext}}$  of 532 nm and an electric field  $|E_0|$  of 1 V/m is incident with an angle of  $35^\circ$  relative to the sample surface. The perfectly matched layers surrounding the volume are set to absorb all outgoing waves. The dielectric constant of the Ag objects is referenced from the literature [63]. The surface normal component of the electric field  $E_z$  is sampled.

A Ag flat plate is placed beneath the tip apex with a gap distance  $d_{\text{FEM}}$ . Here we define the origin of the gap distance ( $d_{\text{FEM}} = 0$ ) as the tip height when the Ag-tip apex forms point contact with the Ag surface. As described above, the quantum-corrected molecular height  $d_{\text{D}_2}^{\text{qc}}$  is calculated to be approximately 0.32–0.33 nm for  $\text{D}_2/\text{Ag}(111)$ . In the  $d_{\text{FEM}}$  definition, taking into account the atomic radius of Ag, the position of the molecule corresponds to  $\sim 0.2$  nm above the Ag surface plane in the FEM model. Although the calculated  $d_{\text{D}_2}^{\text{qc}}$  depends on the tip height [Figs. 3(h) and 3(j) in the main text], in the FEM model, we used the constant height for the sampling point at any gap distances. We confirmed that differences in the  $d_{\text{FEM}}$  definition or the molecular position on the order of 0.1 nm do not result in qualitative differences in the field enhancement factor curves. To directly compare with the experimental TERS intensities, the electric field enhancement factor  $(|E_z|/|E_0|)^4$  (Ref. [64]) is displayed in the plots of Fig. 2(c) in the main text. To the field enhancement of the nearest neighboring molecule, assuming the molecule is placed in the next adsorption site of Ag(111),  $x = 0.29$  nm is used [red triangle in the inset of Fig. 2(c) in the main text]. Thus, when the point at the surface just under the tip is defined as  $(x, y, z) = (0, 0, 0)$ , the black and red curves shown in Fig. 2c of the main text represent the plots sampling at  $(x, y, z) = (0, 0, 0.20)$  nm and  $(0.29, 0, 0.20)$  nm, respectively.

The tip heights in the DFT calculations are comparable with the gap distances with the FEM simulations that reproduced the Raman enhancement [Fig. 2(c) in the main text; the gap distances of 550 to 850 pm in the simulation correspond to the tip height of  $\sim 0.8$  to

$\sim 1.1$  nm, considering the Ag-atom radius].

## II. SUPPLEMENTAL RESULTS AND DISCUSSION

### A. Nuclear Spin Isomers

H<sub>2</sub> and D<sub>2</sub> have two nuclear spin isomers, *ortho* and *para*. *para*-H<sub>2</sub> (nuclear spin quantum number  $I = 0$ ) is more stable than *ortho*-H<sub>2</sub> ( $I = 1$ ) by 14 meV [65]. *para*- (*ortho*-) H<sub>2</sub> has only even (odd) rotational quantum numbers  $J$ . Although *ortho*-H<sub>2</sub> is the predominant species in the gas phase at room temperature (a temperature equilibrium composition of 75%), the molecular adsorption on metals enhances the *ortho*-to-*para* conversion, leading to the dominance of the *para* species on the surfaces [4]. In the TERS spectra, we can detect only *para*-H<sub>2</sub> (Table S2); as a reference, in the gas phase, *ortho*-H<sub>2</sub> have a Raman-active rotational mode  $[(\nu, J) = (0, 1) \rightarrow (0, 3)]$  at  $\sim 587$  cm<sup>-1</sup> [48, 65]. This implies that we detected only the physisorbed species after *ortho*-*para* conversion on the surface. In the case of D<sub>2</sub>, *ortho* ( $I = 0, 2$ ) is more stable than *para* ( $I = 1$ ) by 7.4 meV and more dominant (67%) in the gas phase at room temperature. Only *ortho*-D<sub>2</sub> was detected in our TERS spectra, indicating again that *para*-D<sub>2</sub> was converted on the surface.

Although the dominance of *para*-H<sub>2</sub> in the TERS spectra is consistent with a previous HREELS study of H<sub>2</sub> on a Ag film (0.5–10 L) [8], some previous reports detect *ortho*-H<sub>2</sub> on Ag(111). A HREELS study on H<sub>2</sub>/Ag(111) [66] shows that rotational mode peaks of both *para*-H<sub>2</sub> and *ortho*-H<sub>2</sub> were detected under a higher H<sub>2</sub> pressure ( $9.0 \times 10^{-8}$  Torr) while *para*-H<sub>2</sub> was dominantly detected under a lower pressure ( $2.0 \times 10^{-9}$  Torr). Photostimulated desorption studies (30 L) [12, 13] shows that *ortho*-H<sub>2</sub> and *para*-D<sub>2</sub> are alive on Ag(111) on the order of hundred seconds and that the conversion of D<sub>2</sub> is slower than H<sub>2</sub>.

To compare with the above-mentioned studies, we performed TERS measurements during exposing D<sub>2</sub> to a clean Ag(111) surfaces, as shown in Fig. S2. The gas pressure was set to  $9.7 \times 10^{-8}$  Torr, comparable with the EELS study [66]. The *ortho*-D<sub>2</sub>-derived peaks appeared at  $\sim 16$  L and then saturated at  $\sim 40$  L, while *para*-D<sub>2</sub> was not detected. The weak intensity at low exposures may be due to molecular diffusion along the surface at low coverages and the weak contribution of neighboring molecules to the TERS signal [see Fig. 2(c) in the main text]. It should be noted that even if the gas pressure and exposure values are comparable,

the molecular coverage varies depending on the chamber configuration. Nevertheless, we confirmed that *ortho*-H<sub>2</sub> and *para*-D<sub>2</sub> were not detected at any pressures and exposures we used ( $0.8\text{--}2 \times 10^{-7}$  Torr;  $10^2\text{--}10^3$  Langmuir). The HREELS observation of the metastable isomer only at high exposures [66] may be attributed to be hydrogen multilayers, where the second layer does not interact with the Ag surface. In contrast, the narrow TERS gap for the LT-TERS measurement would suppress the formation of the multiple layers. Another possibility that the metastable isomer were not detected in TERS is that the LSPR in the gap is accelerating the *para-to-ortho* conversion of the molecule under the tip. Although far-field 532-nm irradiation did not affect the conversion rate [13], the strong electric field localized in the STM junction could interact with the nuclear spin of the adsorbate. This effect would be verified through theoretical calculations.

TABLE S2. Frequencies of vibrotational modes of molecular hydrogen detected experimentally (in  $\text{cm}^{-1}$ ). From the TERS results in this study, data from the spectra over-viewing a wide frequency range [“low res.”; Fig. 1(a) in the main text] and from spectra with higher energy resolution [“high res.”; Figs. 3(a)–3(d)] are displayed. Since the vibration frequency of H<sub>2</sub>/Ag(111) is largely red-shifted by the tip proximity, the values at a far tip distance [a relative tip height of  $-110$  pm in Figs. 3(a)–3(d)] are shown as the high resolution data.

System	On Ag(111)	On Ag film	On Cu(001)	Gas phase		
Method	TERS (low res.)	TERS (high res.)	HREELS <sup>a</sup>	HREELS <sup>b</sup>	Raman <sup>c</sup>	Raman <sup>d</sup>
H <sub>2</sub>						
rot	351	348	395	363	354.5	354.365
vib	4121	4134	4178	4178	-	4161.200
rot+vib	4443	-	4533	4517	-	4497.848
D <sub>2</sub>						
rot	169	172	-	177	178.8	179.108
vib	2967	2968	-	3000	2996.1	2993.6
rot+vib	3133	-	-	3170	3166.3	-

<sup>a</sup> Ref. [8].

<sup>b</sup> Ref. [9].

<sup>c</sup> Ref. [67].

<sup>d</sup> Ref. [48].

## B. Excitation Wavelength Dependence

To verify the contribution of LSPR to the TERS intensity, we examined the excitation wavelength ( $\lambda_{\text{exc}}$ ) dependence. Figure S3(a) shows a STML spectrum recorded over a clean Ag(111) surface with a Ag tip. The LSPR results in a broad spectral feature in the visible range with a maximum at  $\sim 560$  nm. After recording the STML, we exposed the surface to the  $\text{D}_2$  gas, conducting TERS measurements with  $\lambda_{\text{exc}} = 532$  and 633 nm [Figs. S3(b) and S3(c), respectively]. The peak intensity of each mode significantly changes with  $\lambda_{\text{exc}}$ , whereas the Raman shift value is unchanged. The vibrational intensity is weakened with  $\lambda_{\text{exc}} = 633$  nm, indicating the corresponding scattering light is not efficiently enhanced by the LSPR because the peak position ( $\lambda_{\text{Raman}} = 779$  nm) is located in the weak resonance range of the LSPR [Fig. S3(a)]. In contrast, both the rotational and vibrational peaks become intense with  $\lambda_{\text{exc}} = 532$  nm because they are more resonant with the LSPR.